catalysts

MDPI

Article

Effect of the Second-Shell Coordination Environment on the Performance of P-Block Metal Single-Atom Catalysts for the Electrosynthesis of Hydrogen Peroxide

Yidi Wu, Yuxiang Zhang and Sen Lin *

State Key Laboratory of Photocatalysis on Energy and Environment, College of Chemistry, Fuzhou University, Fuzhou 350002, China; wuyiddd519@snnu.edu.cn (Y.W.); 221320272@fzu.edu.cn (Y.Z.)
* Correspondence: slin@fzu.edu.cn

Abstract: Hydrogen peroxide (H_2O_2) is an important chemical with a diverse range of industrial applications in chemical synthesis and medical disinfection. The traditional anthraquinone oxidation process, with high energy consumption and complexity, is being replaced by cost-effective and environmentally friendly alternatives. In order to explore suitable catalysts for the electrocatalytic synthesis of H_2O_2, the stability of B,N-doped graphene loaded with various p-block metal (PM) single atoms (i.e., PM-N_xB_y: x and y represent the number of atoms of N and B, respectively) and the effects of different numbers and positions of B dopants in the second coordination shell on the catalytic performance were studied by density functional theory (DFT) calculations. The results show that Ga-N_4B_6 and Sb-N_4B_6 exhibit enhanced stability and $2e^-$ oxygen reduction reaction (ORR) activity and selectivity. Their thermodynamic overpotential η values are 0.01 V, 0.03 V for Ga-N_4B_6's two configurations and 0.02 V, 0 V for Sb-N_4B_6's two configurations. Electronic structure calculations indicate that the PM single atom adsorbs OOH* intermediates and transfers electrons into them, resulting in the activation of the O-O bond, which facilitates the subsequent hydrogenation reaction. In summary, Sb-N_4B_6 and Ga-N_4B_6 exhibit extraordinary $2e^-$ ORR performance, and their predicted activities are comparable to those of known outstanding catalysts (such as $PtHg_4$ alloy). We propose effective strategies on how to enhance the $2e^-$ ORR activities of carbon materials, elucidate the origin of the activity of potential catalysts, and provide insights for the design and development of electrocatalysts that can be used for H_2O_2 production.

Keywords: $2e^-$ ORR; p-block metal single atom; electrocatalysis

Citation: Wu, Y.; Zhang, Y.; Lin, S. Effect of the Second-Shell Coordination Environment on the Performance of P-Block Metal Single-Atom Catalysts for the Electrosynthesis of Hydrogen Peroxide. *Catalysts* **2024**, *14*, 421. https://doi.org/10.3390/catal14070421

Academic Editors: Igor A. Pašti, José R. B. Gomes and Kai S. Exner

Received: 4 June 2024
Revised: 26 June 2024
Accepted: 28 June 2024
Published: 30 June 2024

1. Introduction

Hydrogen peroxide (H_2O_2) is a chemical oxidant that is employed in a wide range of industrial processes. The most environmentally friendly aspect of H_2O_2 is that when it interacts with other substances, it breaks down into H_2O and O_2 without creating other impurities. In particular, the demand for water treatment and environmental remediation requires increased production of H_2O_2. However, the high cost of synthesizing H_2O_2 via the energy-intensive industrial anthraquinone oxidation process [1], as well as the associated costs of storage and transport, represent significant obstacles to further development [2]. Furthermore, this process has a significant negative impact on sustainability, as it generates large amounts of harmful effluents. Consequently, in order for hydrogen peroxide to be more widely and effectively utilized as a green and non-polluting product, the issues surrounding on-site preparation, storage and transportation must be resolved. A method for synthesizing H_2O_2 directly from O_2 and H_2 has been proposed. However, its practical application in factories is limited due to the risk of explosion in H_2/O_2 gas mixtures [3]. Therefore, new methods for H_2O_2 production, including the photocatalytic oxidation of water and the electrocatalytic reduction of oxygen [4,5], have been proposed and have received extensive attention.

The electrocatalytic reduction of oxygen allows the production of H_2O_2 under mild conditions using electrocatalysts. The development of highly active, selective and stable electrocatalysts is the key to the production of H_2O_2 [6]. Currently, platinum (Pt)-based catalysts are the most commonly used catalysts. However, the scarcity and high cost of the starting feedstock Pt have become the factors in limiting its widespread use [7]. To date, the field has concentrated on the investigation of more suitable catalysts, including transition metal oxides [8,9], carbides [10–12], nitrides [13–15], sulfides [16–18] and carbon materials [19–21]. Since the development of Pt_1/FeO_x by Qiao et al. in 2011, single-atom catalysts (SACs) have received considerable attention and have shown encouraging performance in oxygen reduction reactions (ORRs) [22,23], nitrogen reduction reactions (NRRs) [24,25], α,β-unsaturated aldehydes hydrogenation reactions [26], and hydrogen spillover [27,28]. SACs represent an ideal replacement for Pt-based metal catalysts, benefiting from their high atomic utilization, high activity and low cost of the component elements [29–31].

Previous studies have shown that the M-N_4 unit of metal–nitrogen–carbon (M-N-C) catalysts exhibits excellent electrocatalytic activity [32,33]. In recent studies, researchers have introduced a large number of other non-metallic elements (O, B, S, P, etc.) in addition to N. M-N-C was prepared by adjusting the type, number and doping position of heteroatoms (first, second and even higher coordination shells), which artificially modify the partial coordination environment of the metal single atom, thus providing the possibility to improve the electrocatalytic reaction activity [34–36].

Usually, main-group metals are not considered to be catalytically active due to their electron-filled d orbitals (d^{10} orbitals) [37,38]. However, many studies reveal that the main-group metal single atoms can also be activated through local coordination environment engineering of the M-N_x unit, thereby demonstrating that main-group metals may also possess excellent catalytic properties [39,40]. Although p-block metal SACs with activated p-orbital electrons have been shown to be efficient and stable ORR electrocatalysts, previous studies have typically been focused on $4e^-$ ORR [41,42], with only a few studies on $2e^-$ ORR. For example, Zhang et al. [43] uncovered that the selectivity and activity of indium (In) SACs for $2e^-$ ORR could be improved through modulating the first coordination shell layer. Additionally, Gu et al. [44] reported that the introduction of oxygen-functional groups in the second-shell coordination environment could enhance the $2e^-$ and $4e^-$ ORR activity and selectivity of antimony (Sb) SACs (Sb-N_4). These studies suggest that the p-electrons of p-block metals can be activated to catalyze ORR by modulating the local coordination environment.

In this paper, we investigate the catalytic $2e^-$ ORR process on nitrogen-doped graphene (NG) substrates anchored with single atoms of different p-block metals (M = Al, Ga and Sb) using density functional theory (DFT) calculations. The second-shell coordination environment of the M-N_4 site is modified by the introduction of the heteroatom boron (B) to modulate the electronic structure of M. The results demonstrate that B doping optimizes the binding strength of the central metals (Sb and Ga) to the intermediate OOH* during the ORR process, resulting in a neither too strong nor too weak adsorption energy of OOH*. Encouragingly, the predicted activities of Sb-N_4B_6 and Ga-N_4B_6 are comparable to those of known commercial catalysts. The theoretical result demonstrates that the electrocatalytic activity of NG loaded with Sb and Ga single atoms can be enhanced via the introduction of heteroatom B in the second-shell coordination environment. Furthermore, they provide insights into the rational design of efficient catalysts for $2e^-$ ORR.

2. Results and Discussion

2.1. Structures and Stability

To select catalysts that are suitable for the electrochemical synthesis of H_2O_2, three screening criteria are considered: Firstly, SACs must have good stability. Secondly, SACs must have a low overpotential. Thirdly, SACs must be selective for the $2e^-$ ORR compared with the competitive $4e^-$ ORR. A $6 \times 6 \times 1$ supercell of NG was constructed as a model. In order to reduce interactions between adjacent layers in periodically repeated cells, vacuum

thicknesses were set to 15 Å. A metal (Al, Ga and Sb) atom was incorporated into the model to form the central site M-N_4. The heteroatom B was introduced to replace the C atoms in the second coordination shell, thereby forming M-N_4B_X (x = 1–6). The M-N_4B_X model and the locations of B atoms are shown in Figure 1a. The first blue circle in the graphene structure represents the first coordination shell, and the C atoms in the second red circle outside represent the second coordination shell. The coordination regulation of the second shell, as illustrated in Figure S1, allows for the formation of 39 distinct M-N_4B_X structures, each containing varying amounts of B atoms at different sites. This results in a total of 117 catalyst models.

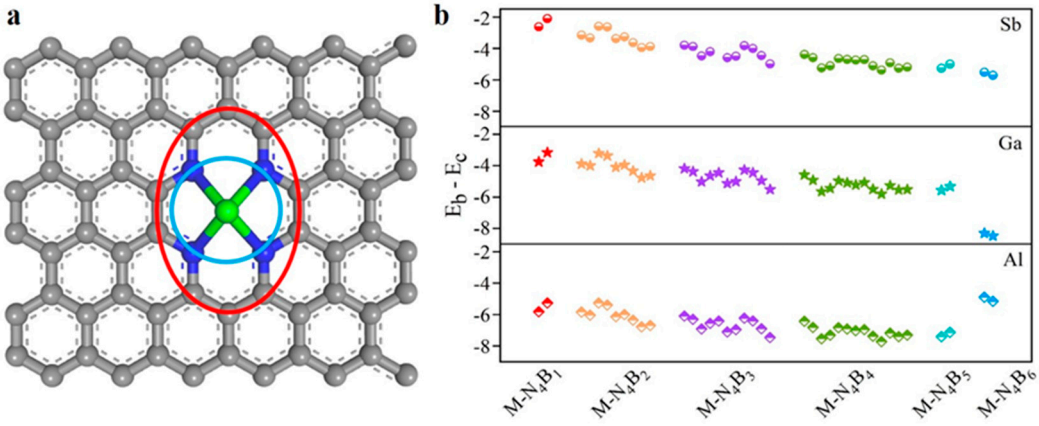

Figure 1. (**a**) A schematic diagram of the M–N_4B_X (X = 1–6) structural model, where the blue circle represents the first coordination layer and the red circle represents the second coordination shell. (**b**) The difference between the binding energy (E_b) and cohesive energy (E_c) of the M-N_4B_X structure, where different (E_b–E_c) values of the same X are owed to the B atoms doped at different sites. The gray, blue and green balls represent the C atom, N atom and p-block metal atoms (Sb, Ga and Al), respectively.

Since the stability of the catalyst is the most fundamental prerequisite for its application, the thermodynamic stability of the catalyst was first evaluated by calculating the binding energy (E_b) between the PM atoms and the adjacent N atoms and the cohesion energy (E_c) of the PM atoms. E_b and E_c are calculated as follows:

$$E_b = E_{M-N_4B_XC} - E_M - E_{N_4B_XC} \quad (1)$$

where $E_{M-N_4B_XC}$, E_M and $E_{N_4B_XC}$ represent the total energy of the catalyst, the energy of the isolated single metal atom and the energy of the catalyst without loading the metal single atom, respectively.

$$E_c = \frac{E_{bulk}}{n} - E_M \quad (2)$$

where E_{bulk} is the total energy of the metal bulk material and n represents the number of metal atoms in the bulk material.

Figure 1b shows the discrepancy between the binding energy and the cohesive energy ($E_b - E_c$). If the difference is less than zero ($E_b - E_c < 0$), the bulk of the metal is more likely to be isolated by M-N_4B_X-C during the reaction rather than agglomerating to form nanoparticles, and thus the structure is stable. The value of ($E_b - E_c$) for all the structures in the figure is less than 0, which means that the three main groups of metals are available to be stably embedded in the hole of NG through the nitrogen–metal (N-M) bonds.

2.2. Activity and Selectivity of the Catalysts

The $4e^-$ ORR reaction pathway is as follows:

$$O_2 + * + H^+ + e^- \rightarrow OOH^*, \quad (3)$$

$$OOH^* + H^+ + e^- \rightarrow H_2O + O^*, \quad (4)$$

$$O^* + H^+ + e^- \rightarrow OH^*, \quad (5)$$

$$OH^* + H^+ + e^- \rightarrow H_2O + *, \quad (6)$$

The complete reaction can be expressed as

$$O_2 + 4H^+ + 4e^- \rightarrow 2H_2O \ (E_0 = 1.23 \text{ V vs. RHE}), \quad (7)$$

The $2e^-$ ORR reaction pathway is as follows:

$$O_2 + * + H^+ + e^- \rightarrow OOH^*, \quad (8)$$

$$OOH^* + H^+ + e^- \rightarrow H_2O_2 + *, \quad (9)$$

The complete reaction can be expressed as

$$O_2 + 2H^+ + 2e^- \rightarrow H_2O_2 \ (E_0 = 0.7 \text{ V vs. RHE}), \quad (10)$$

The ORR process is shown in Figure 2, it can be understood as follows: O_2 adsorbs at the active site, gaining an electron (e^-) and a proton (H^+) from the aqueous solution to produce an OOH* intermediate. OOH* is then reduced by ($H^+ + e^-$), further generating either H_2O_2 ($2e^-$ ORR) or H_2O and O* intermediates ($4e^-$ ORR). The key factor in the synthesis of H_2O_2 is the breaking or non-breaking of the O-O bond. In both the $4e^-$ and $2e^-$ pathways, the intermediate OOH* is formed in the first reaction step of oxygen adsorption and hydrogenation. Therefore, we calculated the free energy of OOH* (G_{OOH^*}) first, as shown in Tables S1–S3. Subsequently, the ORR performance of the M-N_4 site and the M-N_4B_X under acidic conditions (pH = 0) was investigated.

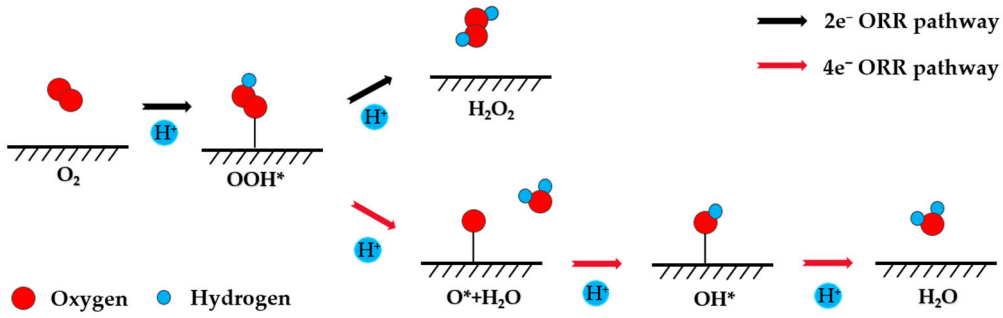

Figure 2. Reaction pathways along with O_2 electroreduction.

The synthesis of H_2O_2 is dependent upon the moderate adsorption strength of the OOH* intermediate on the SACs, which is a critical factor in determining the catalytic performance of the process. The adsorption energy must be neither too strong nor too weak, as this would result in the O-O bond being broken or the subsequent reaction steps being unable to proceed. From Equation 10, it can be seen that the ΔG of each electron step in $2e^-$ ORR is 0.70 eV (G_{OOH^*} = 4.22 eV). Therefore, the ΔG for the entire reaction is 1.40 eV ($G_{H_2O_2}$ = 3.52 eV). Theoretically, the closer the U_L is to the equilibrium potential (0.70 V vs. RHE), the closer the G_{OOH^*} is to 4.22 eV, and the more likely the free energy of all reactions is to be zero, indicating that the catalyst is highly active in the $2e^-$ ORR process. As illustrated in the Tables S1–S4, the differing numbers of B in the second coordination shell and the distinct central atoms exhibit varying adsorption strengths for the intermediate of OOH*.

The ΔG of the entire $2e^-$ ORR process is known to be 1.40 eV. If the free energy of G_{OOH^*} becomes too small, the free energy change of the first electron step will be greater than 1.40 eV ($\Delta G_1 < -1.40$ eV) and $G_{OOH^*} < 3.52$ eV, which causes the ΔG_2 to increase during the thermodynamic reaction ($\Delta G_2 > 0$), and this is thermodynamically unfavorable.

Initially, it is found that the G_{OOH^*} of M-N_4 (M = Sb, Ga, and Al) was less than 4.22 eV, with a significant difference (Table S1). This is not conducive to $2e^-$ ORR, and thus M-N_4 is not suitable to serve as the catalytic site of $2e^-$ ORR.

On the other hand, an examination of Tables S2 and S3 reveals that the G_{OOH^*} of Al-N_4B_X and Ga-N_4B_X is becoming larger in the process of increasing heteroatom B atoms; in addition, the G_{OOH^*} of Al-N_4B_X (X = 1–4) is almost less than 3.52 eV. Consistently, the G_{OOH^*} for all structures is observed to be almost less than 3.52 eV in Ga-N_4B_X. This indicates that in these structures, the intermediate OOH* will be strongly adsorbed at the reaction site, resulting in the O-O bond breaking during the subsequent reaction process, which is not conducive to the synthesis of H_2O_2. Therefore, these structures are unsuitable as catalysts for the $2e^-$ ORR. Furthermore, the G_{OOH^*} of Sb-N_4B_X in Table S4 displays an initial increase and subsequent decrease with the addition of B heteroatoms (G_{OOH^*} rises at X = 1–4 and then declines at X = 5–6). Among the structures, the G_{OOH^*} of Sb-N_4B_4 is almost all greater than 4.92 eV, indicating that Sb-N_4B_4 has difficulty adsorbing OOH* intermediates and activating the O-O bond of OOH*, which is also not conducive to the formation of H_2O_2 by the $2e^-$ ORR process. Therefore, the above structures were screened out via the calculation of the adsorption energy of the OOH* intermediate (Al-N_4B_X, X = 1–4; Ga-N_4B_X, X = 1–3; Sb-N_4B_X, X = 4).

In the remaining models, the U_L values during the ORR were calculated. Figure 3 shows the calculated U_L value for the Al-N_4B_X (X = 5–6), Ga-N_4B_X (X = 4–6) and Sb-N_4B_X (X = 1–3, 5–6) systems. Notably, Ga-N_4B_6 (0.69 V and 0.67 V), Sb-N_4B_1 (0.63 V and 0.59 V), Sb-N_4B_2 (0.49 V and 0.67 V) and Sb-N_4B_6 (0.68 V and 0.70 V) exhibited U_L values that are very close to 0.70 V, indicating that Ga-N_4B_6 and Sb-N_4B_X (X = 1–2, 6) have high activity in the synthesis of H_2O_2. Of these, Ga-N_4B_6 and Sb-N_4B_6 have the highest U_L values and had the highest activity. In addition, the U_L values of Al-N_4B_X (X = 5–6), Ga-N_4B_X (X = 4–5) and Sb-N_4B_X (X = 3, 5) are too small, implying that the activity of these catalysts is quite poor. Therefore, these catalysts will not be further considered.

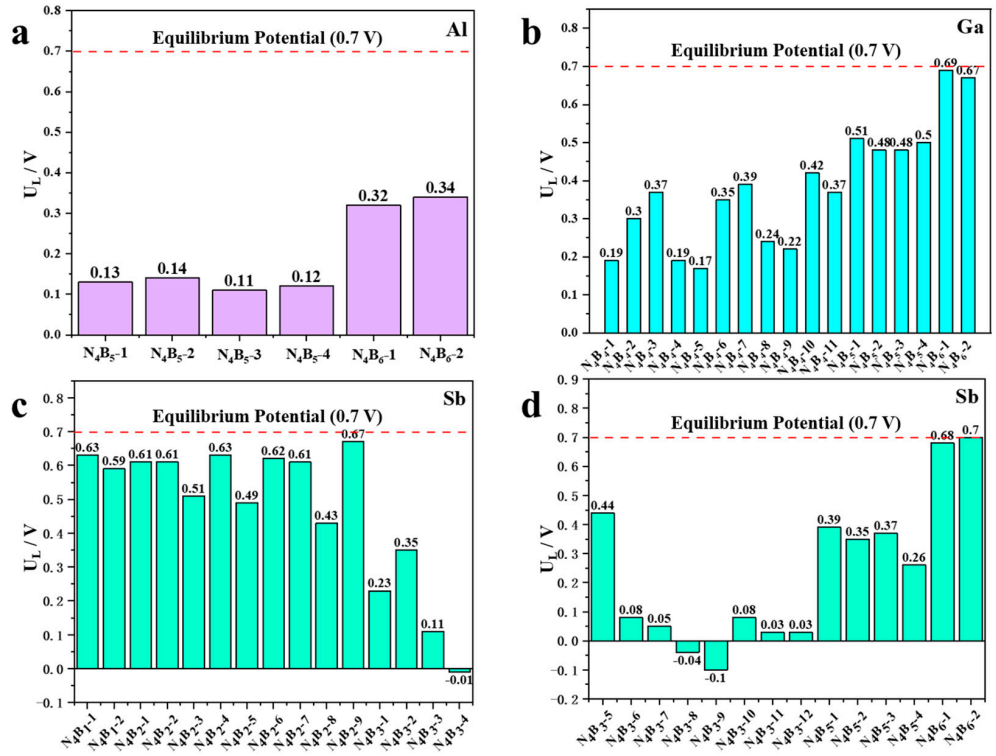

Figure 3. Limiting potential (U_L) of the $2e^-$ ORR on (**a**) Al−N_4B_X (X = 5−6); (**b**) Ga−N_4B_X (X = 4−6); (**c**,**d**) Sb−N_4B_X (X = 1−3, 5−6) catalysts. The red dashed line represents the equilibrium potential which is equal to 0.70 V.

The adsorption strength of the intermediate at the active center on the surface of the catalyst plays an equally essential role in determining the activity and selectivity of the catalytic reaction. Thus, the free energies of ORR at each basic reaction step on Ga-N_4B_6 and Sb-N_4B_6 were calculated, allowing the determination of the η and potential-limiting steps (PDSs). This, in turn, enables the assessment of the ORR selectivity of Ga-N_4B_6 and Sb-N_4B_6. The reaction free-energy profiles of the 2e⁻ ORR and 4e⁻ ORR on Ga-N_4B_6 and Sb-N_4B_6 are shown in Figure 4.

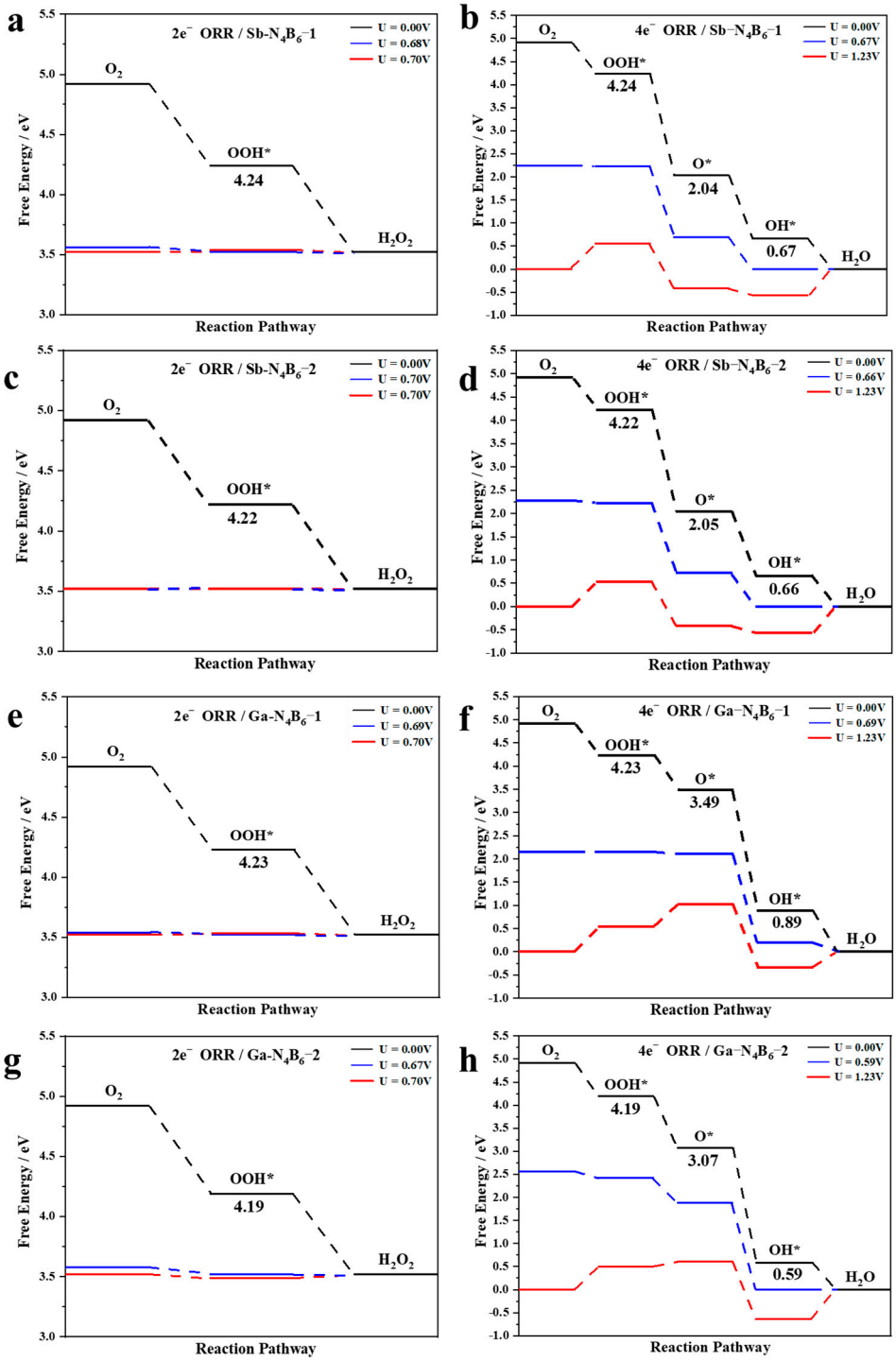

Figure 4. The Gibbs free−energy diagrams on (**a**–**d**) Sb−N_4B_6 and (**e**–**h**) Ga−N_4B_6 of 2e⁻ ORR and 4e⁻ ORR.

As shown in Figure 4a,c, for the 2e$^-$ pathway on Sb-N_4B_6, the minimum ΔG value at U = 0.00 V is 0.68 eV and 0.70 eV. However, for the structure of Sb-N_4B_6-1, the hydrogenation of the O_2 adsorbed at the central site on the catalyst surface to form OOH* intermediate represents a PDS of the entire 2e$^-$ ORR process. Nevertheless, for Sb-N_4B_6-2, any step during the reaction can be a PDS. This allows the 2e$^-$ ORR process to be carried out spontaneously on Sb-N_4B_6 at U = 0.68 V and 0.70 V, without the need for additional energy input. According to Formula (3), the η of Sb-N_4B_6-1 and Sb-N_4B_6-2 can be calculated to be 0.02 V and 0 V, respectively. For the 4e$^-$ ORR process (Figure 4b,d), the minimum ΔG was calculated at U = 0.00 V to be 0.67 eV and 0.66 eV, which is the last step of the 4e$^-$ ORR process. This indicates that the hydrogenation of OH* to form H_2O is a PDS for Sb-N_4B_6-1 and Sb-N_4B_6-2. All of the reaction steps occurred spontaneously at 0.67 V and 0.66 V, respectively. Consequently, the η value of the 4e$^-$ ORR (0.56 V and 0.57 V) is greater than that of the 2e$^-$ ORR (0.02V and 0 V). The calculation results indicate that Sb-N_4B_6 is more likely to form H_2O_2 via the 2e$^-$ ORR pathway than to produce H_2O via the 4e$^-$ ORR pathway. This indicates that Sb-N_4B_6 exhibits high selectivity for 2e$^-$ ORR. Similarly, for Ga-N_4B_6, during the 2e$^-$ ORR process, the PDSs are the first and second steps, with a value of ΔG to be 0.69 eV and 0.67 eV, respectively. The corresponding η is 0.01 and 0.03 V, respectively. During the 4e$^-$ ORR, the PDSs are the first and fourth steps, with ΔG values of 0.69 eV and 0.59 eV, respectively. The corresponding η is 0.54 V and 0.65 V, respectively. The η of the 4e$^-$ ORR obtained by Ga-N_4B_6 (0.54 and 0.65 V) was larger than that of 2e$^-$ ORR (0.01 and 0.03 V), and Ga-N_4B_6 also demonstrated a preference for the 2e$^-$ ORR pathway over the 4e$^-$ ORR pathway, resulting in the formation of H_2O_2 rather than H_2O. In general, Sb-N_4B_6 and Ga-N_4B_6 are more selective for 2e$^-$ ORR than 4e$^-$ ORR, and thus they are ideal catalysts for H_2O_2 synthesis. Moreover, the performance of Sb-N_4B_6 was slightly superior to that of Ga-N_4B_6. More importantly, the predicted activity of Sb-N_4B_6 and Ga-N_4B_6 is comparable to that of known outstanding electrocatalysts for H_2O_2 production, for example, the $PtHg_4$ alloy [6].

2.3. ORR Activity Origin

Essentially, the properties of catalysts, such as activity, stability and selectivity, are typically influenced by the combined effects of geometry and electronic structure. In the previous section, the effect of the geometry on the 2e$^-$ ORR activity and selectivity was elucidated in detail. To gain a deeper understanding of the nature of the catalyst activity, the origin of the catalyst activity is discussed through an analysis of the electronic structure. In this process, a bridge is needed to connect the activity and electronic information. In the preceding discussion of thermodynamics, the adsorption free energies of the reaction and intermediates play a crucial role in the activity and selectivity, corresponding with the micro-changes (e.g., the number of valence electrons, d-band center, p-band center, electron spin and others) of the active metals.

The key factors responsible for the excellent activity and selectivity of Sb-N_4B_6 and Ga-N_4B_6 SACs were identified through an electronic structure analysis. A Bader charge and charge differential density (CDD) analysis were conducted to quantitatively determine the charge transfer that occurs upon adsorption of the reaction intermediate. As illustrated in Figure 5, the results indicate that there is a significant electron transfer between both Sb and Ga with N atoms of Sb-N_4B_6 and Ga-N_4B_6. The Bader charge analysis revealed that about 1.53 e$^-$ transferred to the substrate N atoms from Sb in Sb-N_4B_6-1 and Sb-N_4B_6-2, respectively. Furthermore, the CDD plot (Figure 5a,b) showed that there was a significant charge transfer between Sb and OOH* when OOH* adsorbed to Sb-N4B_6-1 and Sb-N_4B_6-2, with about 0.53 and 0.54 e$^-$ from Sb to the adsorbed OOH, respectively. This leads to an elongation of the O-O bond length of the OOH* from 1.21 Å to 1.475 Å and 1.48 Å (Table 1). The calculation result implies that the Sb single atom effectively activates the O-O bond, thereby facilitating the subsequent hydrogenation of OOH* to generate the final H_2O_2 product. There are approximately 0.43 and 0.47 e$^-$ transferred from Ga to adsorbed OOH* in the same Ga-N_4B_6-1 and Ga-N_4B_6-2 (Figure 5c,d), respectively, resulting

in the O-O bond lengths of OOH* being elongated to 1.44 Å and 1.45 Å (Table 1). Thus, the analysis demonstrated that both Sb-N_4B_6 and Ga-N_4B_6 exhibit good ORR activity and predominantly followed the $2e^-$ pathway during the reaction. The understanding of the activity origin can provide insights at the molecular level into the catalytic process, thereby enabling the design of catalysts with optimal performance. It is noteworthy that the curvature of graphene can influence the catalytic performance, as reported in previous studies [45,46], and it may be interesting to investigate the "curvature effect" of electrocatalysis in our future work.

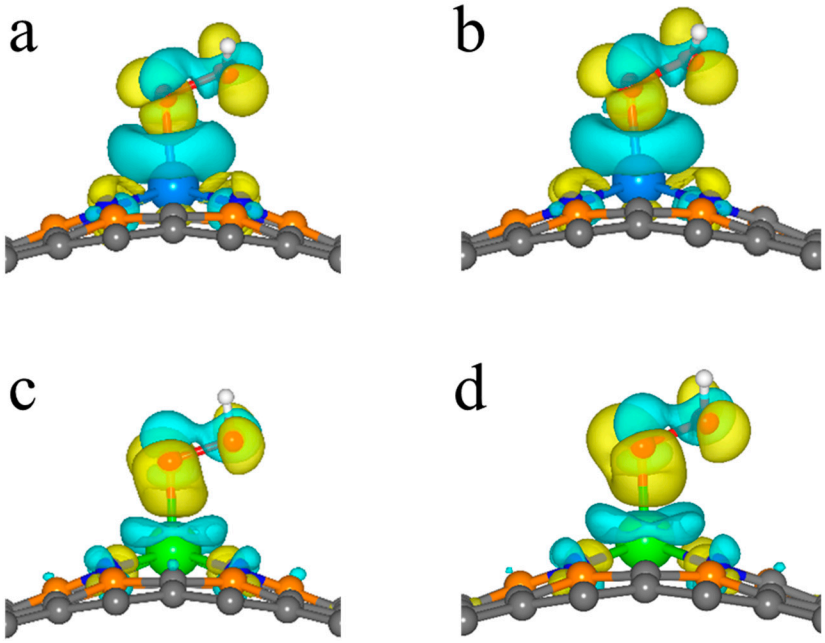

Figure 5. The charge differential density (CDD) diagram of OOH* adsorbed on M-N_4B_6: (**a**) Sb-N_4B_6-1; (**b**) Sb-N_4B_6-2; (**c**) Ga-N_4B_6-1; (**d**) Ga-N_4B_6-2. Grey ball: C; orange ball: B; red ball: O; white ball: H; blue ball: Sb; green ball: Ga. The isosurface value is set to 0.003 e/Bohr^3.

Table 1. Bader charges before the center of the metal adsorption OOH (q_M (e^-)) after (Q_M (e^-)) lost charge; OOH* intermediates of charge are (q_{OOH} (e^-)) and O-O bond length.

M-N_4B_6	q_M (e^-)	Q_M (e^-)	q_{OOH} (e^-)	Bond Length (Å)
Ga-N_4B_6-1	−1.48	−1.57	0.43	1.44
Ga-N_4B_6-2	−1.45	−1.57	0.47	1.45
Sb-N_4B_6-1	−1.53	−2.30	0.53	1.475
Sb-N_4B_6-2	−1.53	−2.32	0.54	1.48

3. Computational Methods

All the spin-polarized DFT calculations were performed using the Vienna ab initio simulation package (VASP.5.4.4) [47]. The projector-augmented-wave (PAW) potential was employed for modeling the interactions between ions and electrons, with a plane wave energy cutoff set to 450 eV [48,49]. The exchange correlation potential was treated by the Perdew–Burke–Ernzerhof (PBE) version of generalized gradient approximation (GGA) [50]. The k-point grid was set to $3 \times 3 \times 1$ for structural optimization and also for sampling of the Brillouin region in electronic structure calculations. The zero-damping DFT-D3 method [51] proposed by Grimme et al. [52] was used to describe the van der Waals interactions. The convergence standard of energy was set at 10^{-4} eV, and all structures were relaxed until the forces on each ion were less than 0.05 eV/Å.

Based on Nørskov's computational hydrogen electrode model [53,54], we calculated the Gibbs free energy change (ΔG) for each elementary step as follows:

$$\Delta G = \Delta E + \Delta E_{zpe} - T\Delta S + eU, \quad (11)$$

where ΔE is the energy difference directly calculated by DFT before and after each elementary reaction step; ΔE_{zpe} and TΔS are the differences in the zero-point energies and entropy at 298.15 K, respectively; and the value of eU is determined by the applied potential (U). In addition, VASPKIT [55] was used to perform vibrational frequency analysis to obtain ΔEzpe and ΔS values.

In addition, we defined a descriptor of limiting potential (U_L) to describe the activity of the electrocatalytic ORR with the free energy change of the potential-determining step (PDS):

$$U_L = -\Delta G_{PDS}/e, \quad (12)$$

where the ΔG_{PDS} is the Gibbs free energy change of the PDS.

The overpotential (η) was calculated as

$$\eta = U_{equilibrium} - U_L, \quad (13)$$

where the equilibrium potentials ($U_{equilibrium}$) are 1.23 V and 0.70 V for the $4e^-$ ORR and $2e^-$ ORR, respectively.

4. Conclusions

In this work, the $2e^-$ ORR performance of a series of PM-N_4B_X/C (PM = Al, Ga and Sb) catalysts in an acidic environment is investigated in terms of catalytic activity and product selectivity by DFT calculations. The results show that Sb-N_4B_6 and Ga-N_4B_6 have good stability and high activity and selectivity for $2e^-$ ORR, and Al-N_xB_y catalysts are all screened out due to their poor activity. In order to ascertain the origin of the catalytic activity, the electronic structure of the OOH* intermediates adsorbed on the two catalysts was calculated. The results revealed that electrons are transferred from the central atom into OOH*, which activates the O-O bond and facilitates continued hydrogenation. These findings elucidate the origin of the exceptional $2e^-$ ORR electrocatalytic activity of Sb-N_4B_6 and Ga-N_4B_6. This work offers theoretical insights into the rational design of efficient catalysts for H_2O_2 synthesis.

Supplementary Materials: The following supporting information can be downloaded at https://www.mdpi.com/article/10.3390/catal14070421/s1, Figure S1: All of the possible M−N_4B_X (X=1−6) structures doped by different amounts of B at different sites models; Table S1: The G of OOH* on M−N_4, G means G_{OOH^*}; Table S2: The G of OOH* on Al−N_4B_X, G means G_{OOH^*}; Table S3: The G of OOH* on Ga−N_4B_X, G means G_{OOH^*}; Table S4: The G of OOH* on Sb−N_4B_X, G means G_{OOH^*}.

Author Contributions: Y.W. designed the calculations. S.L. supervised the project. Y.W. and Y.Z. performed the calculations. All authors discussed the experiments and results. Y.W., Y.Z. and S.L. prepared and revised the manuscript. All authors have read and agreed to the published version of the manuscript.

Funding: This research was funded by the National Natural Science Foundation of China, grant number 22373017.

Data Availability Statement: Data are contained within the article and Supplementary Materials.

Acknowledgments: The computations were performed at the Hefei Advanced Computing Center and the Supercomputing Center of Fujian.

Conflicts of Interest: The authors declare no conflicts of interest.

References

1. Choi, C.H.; Kim, M.; Kwon, H.C.; Cho, S.J.; Yun, S.; Kim, H.-T.; Mayrhofer, K.J.J.; Kim, H.; Choi, M. Tuning selectivity of electrochemical reactions by atomically dispersed platinum catalyst. *Nat. Commun.* **2016**, *7*, 10922. [CrossRef]
2. Yang, S.; Verdaguer-Casadevall, A.; Arnarson, L.; Silvioli, L.; Čolić, V.; Frydendal, R.; Rossmeisl, J.; Chorkendorff, I.; Stephens, I.E.L. Toward the Decentralized Electrochemical Production of H_2O_2: A Focus on the Catalysis. *ACS Catal.* **2018**, *8*, 4064–4081. [CrossRef]
3. Samanta, C. Direct synthesis of hydrogen peroxide from hydrogen and oxygen: An overview of recent developments in the process. *Appl. Catal. A Gen.* **2008**, *350*, 133–149. [CrossRef]
4. Viswanathan, V.; Hansen, H.A.; Rossmeisl, J.; Nørskov, J.K. Unifying the $2e^-$ and $4e^-$ Reduction of Oxygen on Metal Surfaces. *J. Phys. Chem. Lett.* **2012**, *3*, 2948–2951. [CrossRef] [PubMed]
5. Pan, J.; Fang, Q.; Xia, Q.; Hu, A.; Sun, F.; Zhang, W.; Yu, Y.; Zhuang, G.; Jiang, J.; Wang, J. Dual effect of the coordination field and sulphuric acid on the properties of a single-atom catalyst in the electrosynthesis of H_2O_2. *Phys. Chem. Chem. Phys.* **2021**, *23*, 21338–21349. [CrossRef]
6. Siahrostami, S.; Verdaguer-Casadevall, A.; Karamad, M.; Deiana, D.; Malacrida, P.; Wickman, B.; Escudero-Escribano, M.; Paoli, E.A.; Frydendal, R.; Hansen, T.W.; et al. Enabling direct H_2O_2 production through rational electrocatalyst design. *Nat. Mater.* **2013**, *12*, 1137–1143. [CrossRef] [PubMed]
7. Hu, S.; Qu, X.; Li, P.; Wang, F.; Li, Q.; Song, L.; Zhao, Y.; Kang, X. Photocatalytic oxygen reduction to hydrogen peroxide over copper doped graphitic carbon nitride hollow microsphere: The effect of Cu(I)-N active sites. *Chem. Eng. J.* **2018**, *334*, 410–418. [CrossRef]
8. Zhu, Z.; Pan, H.; Murugananthan, M.; Gong, J.; Zhang, Y. Visible light-driven photocatalytically active g-C3N4 material for enhanced generation of H2O2. *Appl. Catal. B Environ.* **2018**, *232*, 19–25. [CrossRef]
9. Zhou, W.; Xie, L.; Gao, J.; Nazari, R.; Zhao, H.; Meng, X.; Sun, F.; Zhao, G.; Ma, J. Selective H_2O_2 electrosynthesis by O-doped and transition-metal-O-doped carbon cathodes via O_2 electroreduction: A critical review. *Chem. Eng. J.* **2021**, *410*, 128368. [CrossRef]
10. Morozan, A.; Jousselme, B.; Palacin, S. Low-platinum and platinum-free catalysts for the oxygen reduction reaction at fuel cell cathodes. *Energy Environ. Sci.* **2011**, *4*, 1238–1254. [CrossRef]
11. Coleman, E.J.; Co, A.C. The Complex Inhibiting Role of Surface Oxide in the Oxygen Reduction Reaction. *ACS Catal.* **2015**, *5*, 7299–7311. [CrossRef]
12. Wang, Y.; Li, J.; Wei, Z. Transition-metal-oxide-based catalysts for the oxygen reduction reaction. *J. Mater. Chem. A* **2018**, *6*, 8194–8209. [CrossRef]
13. An, G.-H.; Lee, Y.-G.; Ahn, H.-J. Multi-active sites of iron carbide nanoparticles on nitrogen@cobalt-doped carbon for a highly efficient oxygen reduction reaction. *J. Alloys Compd.* **2018**, *746*, 177–184. [CrossRef]
14. Reda, M.; Hansen, H.A.; Vegge, T. DFT Study of the Oxygen Reduction Reaction on Carbon-Coated Iron and Iron Carbide. *ACS Catal.* **2018**, *8*, 10521–10529. [CrossRef]
15. Sun, T.; Jiang, Y.; Wu, Q.; Du, L.; Zhang, Z.; Yang, L.; Wang, X.; Hu, Z. Is iron nitride or carbide highly active for oxygen reduction reaction in acidic medium? *Catal. Sci. Technol.* **2017**, *7*, 51–55. [CrossRef]
16. Fritz, K.E.; Yan, Y.; Suntivich, J. Influence of 3d transition-metal substitution on the oxygen reduction reaction electrocatalysis of ternary nitrides in acid. *Nano Res.* **2019**, *12*, 2307–2312. [CrossRef]
17. Jing, S.; Luo, L.; Yin, S.; Huang, F.; Jia, Y.; Wei, Y.; Sun, Z.; Zhao, Y. Tungsten nitride decorated carbon nanotubes hybrid as efficient catalyst supports for oxygen reduction reaction. *Appl. Catal. B Environ.* **2014**, *147*, 897–903. [CrossRef]
18. Kreider, M.E.; Gallo, A.; Back, S.; Liu, Y.; Siahrostami, S.; Nordlund, D.; Sinclair, R.; Nørskov, J.K.; King, L.A.; Jaramillo, T.F. Precious Metal-Free Nickel Nitride Catalyst for the Oxygen Reduction Reaction. *ACS Appl. Mater. Interfaces* **2019**, *11*, 26863–26871. [CrossRef] [PubMed]
19. Gautam, J.; Tran, D.T.; Singh, T.I.; Kim, N.H.; Lee, J.H. Mesoporous iron sulfide nanoparticles anchored graphene sheet as an efficient and durable catalyst for oxygen reduction reaction. *J. Power Sources* **2019**, *427*, 91–100. [CrossRef]
20. Wang, Y.-Y.; Chen, D.-J.; Tong, Y.J. Mechanistic Insight into Sulfide-Enhanced Oxygen Reduction Reaction Activity and Stability of Commercial Pt Black: An in Situ Raman Spectroscopic Study. *ACS Catal.* **2016**, *6*, 5000–5004. [CrossRef]
21. Guo, X.; Lin, S.; Gu, J.; Zhang, S.; Chen, Z.; Huang, S. Simultaneously Achieving High Activity and Selectivity toward Two-Electron O_2 Electroreduction: The Power of Single-Atom Catalysts. *ACS Catal.* **2019**, *9*, 11042–11054. [CrossRef]
22. Baughman, R.H.; Eckhardt, H.; Kertesz, M. Structure-property predictions for new planar forms of carbon: Layered phases containing sp2 and sp atoms. *J. Chem. Phys.* **1987**, *87*, 6687–6699. [CrossRef]
23. Lian, K.; Wan, Q.; Jiang, R.; Lin, S. Electrocatalytic Oxygen Reduction to Hydrogen Peroxide on Graphdiyne-Based Single-Atom Catalysts: First-Principles Studies. *Catalysts* **2023**, *13*, 307. [CrossRef]
24. Lin, L.; Ma, R.; Jiang, R.; Lin, S. Design of high performance nitrogen reduction electrocatalysts by doping defective polyoxometalate with a single atom promoter. *Phys. Chem. Chem. Phys.* **2024**, *26*, 8494–8503. [CrossRef] [PubMed]
25. Xie, K.; Wang, F.; Wei, F.; Zhao, J.; Lin, S. Revealing the Origin of Nitrogen Electroreduction Activity of Molybdenum Disulfide Supported Iron Atoms. *J. Phys. Chem. C* **2022**, *126*, 5180–5188. [CrossRef]
26. Ge, B.; Wei, F.; Wan, Q.; Zhang, H.; Yuan, P.; Lin, S. Peripheral Coordination-Dependent Descriptor for Selective Interactions between Near-Frontier Molecular Orbitals and Single-Atom Catalysts. *Precis. Chem.* **2023**, *1*, 429–436. [CrossRef]

27. Gu, K.; Lin, S. Sustained Hydrogen Spillover on Pt/Cu(111) Single-Atom Alloy: Dynamic Insights into Gas-Induced Chemical Processes. *Angew. Chem. Int. Ed.* **2023**, *62*, e202312796. [CrossRef] [PubMed]
28. Tan, Z.; Chen, J.; Lin, S. Theoretical Insights into H_2 Activation and Hydrogen Spillover on Near-Surface Alloys with Embedded Single Pt Atoms. *ACS Catal.* **2024**, *14*, 2194–2201. [CrossRef]
29. Yan, B.; Krishnamurthy, D.; Hendon, C.H.; Deshpande, S.; Surendranath, Y.; Viswanathan, V. Surface Restructuring of Nickel Sulfide Generates Optimally Coordinated Active Sites for Oxygen Reduction Catalysis. *Joule* **2017**, *1*, 600–612. [CrossRef]
30. Guo, D.; Shibuya, R.; Akiba, C.; Saji, S.; Kondo, T.; Nakamura, J. Active sites of nitrogen-doped carbon materials for oxygen reduction reaction clarified using model catalysts. *Science* **2016**, *351*, 361–365. [CrossRef]
31. Yang, L.; Jiang, S.; Zhao, Y.; Zhu, L.; Chen, S.; Wang, X.; Wu, Q.; Ma, J.; Ma, Y.; Hu, Z. Boron-Doped Carbon Nanotubes as Metal-Free Electrocatalysts for the Oxygen Reduction Reaction. *Angew. Chem. Int. Ed.* **2011**, *50*, 7132–7135. [CrossRef] [PubMed]
32. Li, F.; Han, G.-F.; Noh, H.-J.; Kim, S.-J.; Lu, Y.; Jeong, H.Y.; Fu, Z.; Baek, J.-B. Boosting oxygen reduction catalysis with abundant copper single atom active sites. *Energy Environ. Sci.* **2018**, *11*, 2263–2269. [CrossRef]
33. Song, P.; Luo, M.; Liu, X.; Xing, W.; Xu, W.; Jiang, Z.; Gu, L. Zn Single Atom Catalyst for Highly Efficient Oxygen Reduction Reaction. *Adv. Funct. Mater.* **2017**, *27*, 1700802. [CrossRef]
34. Wang, Y.; Yuan, H.; Li, Y.; Chen, Z. Two-dimensional iron-phthalocyanine (Fe-Pc) monolayer as a promising single-atom-catalyst for oxygen reduction reaction: A computational study. *Nanoscale* **2015**, *7*, 11633–11641. [CrossRef] [PubMed]
35. Bin Yang, H.; Hung, S.-F.; Liu, S.; Yuan, K.; Miao, S.; Zhang, L.; Huang, X.; Wang, H.-Y.; Cai, W.; Chen, R.; et al. Atomically dispersed Ni(i) as the active site for electrochemical CO2 reduction. *Nat. Energy* **2018**, *3*, 140–147. [CrossRef]
36. Chung, H.T.; Cullen, D.A.; Higgins, D.; Sneed, B.T.; Holby, E.F.; More, K.L.; Zelenay, P. Direct atomic-level insight into the active sites of a high-performance PGM-free ORR catalyst. *Science* **2017**, *357*, 479–484. [CrossRef] [PubMed]
37. Sun, T.; Mitchell, S.; Li, J.; Lyu, P.; Wu, X.; Pérez-Ramírez, J.; Lu, J. Design of Local Atomic Environments in Single-Atom Electrocatalysts for Renewable Energy Conversions. *Adv. Mater.* **2021**, *33*, e2003075. [CrossRef] [PubMed]
38. Tang, C.; Chen, L.; Li, H.; Li, L.; Jiao, Y.; Zheng, Y.; Xu, H.; Davey, K.; Qiao, S.-Z. Tailoring Acidic Oxygen Reduction Selectivity on Single-Atom Catalysts via Modification of First and Second Coordination Spheres. *J. Am. Chem. Soc.* **2021**, *143*, 7819–7827. [CrossRef]
39. Jia, Y.; Yao, X. Atom-Coordinated Structure Triggers Selective H2O2 Production. *Chem* **2020**, *6*, 548–550. [CrossRef]
40. Liu, S.; Li, Z.; Wang, C.; Tao, W.; Huang, M.; Zuo, M.; Yang, Y.; Yang, K.; Zhang, L.; Chen, S.; et al. Turning main-group element magnesium into a highly active electrocatalyst for oxygen reduction reaction. *Nat. Commun.* **2020**, *11*, 938. [CrossRef]
41. Chen, Z.; Song, Y.; Cai, J.; Zheng, X.; Han, D.; Wu, Y.; Zang, Y.; Niu, S.; Liu, Y.; Zhu, J.; et al. Tailoring the d-Band Centers Enables Co_4N Nanosheets To Be Highly Active for Hydrogen Evolution Catalysis. *Angew. Chem. Int. Ed.* **2018**, *57*, 5076–5080. [CrossRef] [PubMed]
42. Wang, T.; Wang, Q.; Wang, Y.; Da, Y.; Zhou, W.; Shao, Y.; Li, D.; Zhan, S.; Yuan, J.; Wang, H. Atomically Dispersed Semimetallic Selenium on Porous Carbon Membrane as an Electrode for Hydrazine Fuel Cells. *Angew. Chem. Int. Ed.* **2019**, *58*, 13466–13471. [CrossRef] [PubMed]
43. Teng, Z.; Zhang, Q.; Yang, H.; Kato, K.; Yang, W.; Lu, Y.-R.; Liu, S.; Wang, C.; Yamakata, A.; Su, C.; et al. Atomically dispersed antimony on carbon nitride for the artificial photosynthesis of hydrogen peroxide. *Nat. Catal.* **2021**, *4*, 374–384. [CrossRef]
44. Wang, T.; Cao, X.; Qin, H.; Shang, L.; Zheng, S.; Fang, F.; Jiao, L. *P*-Block Atomically Dispersed Antimony Catalyst for Highly Efficient Oxygen Reduction Reaction. *Angew. Chem. Int. Ed.* **2021**, *60*, 21237–21241. [CrossRef] [PubMed]
45. Wen, H.; Zhao, Z.; Luo, Z.; Wang, C. Unraveling the Impact of Curvature on Electrocatalytic Performance of Carbon Materials: A State-of-the-Art Review. *ChemSusChem* **2024**, *17*, e202301859. [CrossRef] [PubMed]
46. Wan, Q.; Guo, H.; Lin, S. Corrugation-Induced Active Sites on Pristine Graphene for H_2 Activation. *ACS Catal.* **2022**, *12*, 14601–14608. [CrossRef]
47. Kresse, G.; Hafner, J. Ab initio molecular dynamics for liquid metals. *J. Phys. Rev. B Condens. Matter* **1993**, *47*, 558–561. [CrossRef] [PubMed]
48. Kresse, G.; Joubert, D. From ultrasoft pseudopotentials to the projector augmented-wave method. *Phys. Rev. B* **1999**, *59*, 1758–1775. [CrossRef]
49. Blöchl, P.E. Projector augmented-wave method. *Phys. Rev. B Condens. Matter* **1994**, *50*, 17953–17979. [CrossRef]
50. Perdew, J.P.; Burke, K.; Ernzerhof, M. Generalized gradient approximation made simple. *Phys. Rev. Lett.* **1996**, *77*, 3865–3868. [CrossRef]
51. Sharada, S.M.; Karlsson, R.K.B.; Maimaiti, Y.; Voss, J.; Bligaard, T. Adsorption on transition metal surfaces: Transferability and accuracy of DFT using the ADS41 dataset. *Phys. Rev. B* **2019**, *100*, 035439. [CrossRef]
52. Grimme, S.; Antony, J.; Ehrlich, S.; Krieg, H. A consistent and accurate ab initio parametrization of density functional dispersion correction (DFT-D) for the 94 elements H-Pu. *J. Chem. Phys.* **2010**, *132*, 154104–154119. [CrossRef] [PubMed]
53. Nørskov, J.K.; Rossmeisl, J.; Logadottir, A.; Lindqvist, L.; Kitchin, J.R.; Bligaard, T.; Jónsson, H. Origin of the Overpotential for Oxygen Reduction at a Fuel-Cell Cathode. *J. Phys. Chem. B* **2004**, *108*, 17886–17892. [CrossRef]

54. Valdés, Á.; Qu, Z.-W.; Kroes, G.-J.; Rossmeisl, J.; Nørskov, J.K. Oxidation and Photo-Oxidation of Water on TiO_2 Surface. *J. Phys. Chem. C* **2008**, *112*, 9872–9879. [CrossRef]
55. Wang, V.; Xu, N.; Liu, J.-C.; Tang, G.; Geng, W.-T. VASPKIT: A user-friendly interface facilitating high-throughput computing and analysis using VASP code. *Comput. Phys. Commun.* **2021**, *267*, 108033. [CrossRef]